E23 + E91

PUB-78-103-E
E-0002
E-0281

FERMILAB-78-103-E

Submitted to Phys. Rev.

Study of Δ^{++} Production in π^-p Interactions at 100, 200 and 360 GeV/c*

P.D. Higgins, N.N. Biswas, J.M. Bishop, R.L. Bolduc, N.M. Cason, V.P. Kenney, R.C. Ruchti, and W.D. Shephard
Department of Physics
University of Notre Dame, Notre Dame, Indiana 46556

W.D. Walker, J.S. Loos, L.R. Fortney, A.T. Goshaw, and W.J. Robertson
Department of Physics
Duke University, Durham, N.C. 27706

E.W. Anderson, H.B. Crawley, A. Firestone, R. Floyd†, W.J. Kernan, J.W. Lamsa, and D.L. Parker
Department of Physics
Iowa State University, Ames, Iowa 50010

G.A. Snow
Department of Physics and Astronomy
University of Maryland, College Park, Maryland 20742

B.Y. Oh, M. Pratap, G. Stamkhides, G.A. Smith, and J. Whitmore
Department of Physics
Michigan State University, E. Lansing, Michigan 48824

V. Sreedhar, G. Lavman, B.M. Schwarzschild, and T.S. Yoon
Department of Physics
University of Toronto, Toronto, Ontario M5S 1A7, Canada

G. Hartner and P.M. Patel
Department of Physics
McGill University, Montreal, Quebec H3C 3G1, Canada

L. Voyvodic and R.J. Walker
Fermi National Laboratory
Batavia, Illinois 60510

* Supported in part by the National Science Foundation

† Present address: University of California at Berkeley, Berkeley, California 94720

Abstract

We present a systematic study of Δ^{++} production in π^-p reactions at Fermilab energies. Inclusive and semi-inclusive $\Delta^{++}(1232)$ production cross sections are determined. We observe these cross sections to be energy independent. The invariant cross sections as a function of Feynman x and p_T^2 are also energy independent consistent with scaling behavior. We show that Δ^{++} production is consistent with a one-pion-exchange mechanism. Comparison of the density matrix elements with model predictions and results of a triple-Regge analysis both support the validity of a one-pion-exchange model.

I. Introduction

We present here a systematic study of the inclusive and semi-inclusive production of the $\Delta^{++}(1232)$ baryon in π^-p interactions at Fermilab energies,

$$\pi^-p \rightarrow \Delta^{++} + \text{anything}. \qquad (1)$$

The results of our study of this reaction at 200 GeV/c have recently been reported[1]. For this analysis we also incorporate data from π^-p experiments at 100 and 360 GeV/c. In order to study the energy dependence of reaction (1) we have analyzed the data for all three energies using the same procedure.

In section II, we discuss briefly the experimental method, the data samples, and the kinematics of Δ^{++} production. We present inclusive and semi-inclusive Δ^{++} production cross sections in section III. In section IV we consider the contribution to the Δ^{++} cross section from the decay of higher-mass diffractive states. Invariant differential cross sections in terms of Feynman x and p_T^2 are shown in section V.

In section VI we discuss the Δ^{++} production mechanism in terms of density matrix elements and the triple-Regge model. Our results are then summarized in section VII.

II. Experimental Method

These experiments were all performed at the Fermi National Accelerator Laboratory utilizing the 30-inch Hydrogen Bubble Chamber - Wide Gap Spark Chamber Hybrid system. The events occuring in the bubble chamber were scanned and then measured. The measurements were processed through the geometry program TVGP for spatial reconstruction. Data from the Wide Gap Spark Chambers were also used in determining momenta for fast-forward secondaries.

For this analysis a sample of 29,000 events of all charge multiplicities (ranging from 2-30 charged particles) was available at 360 GeV/c. Additional samples of 17,000 events at 200 GeV/c and 7,700 events at 100 GeV/c were also available. Details of the experiments are discussed elsewhere[2, 3, 4].

Proton identification is based on ionization information for positively charged particles with laboratory momenta ≤ 1.4 GeV/c. All particles which have momenta greater than 1.4 GeV/c and do not decay are assumed to be pions.

For a Δ^{++} to be identified in our experiment, its production and decay configuration must be such that the final proton is identified. In Fig. 1 we show the boundaries imposed for two values of t, the square of the four-momentum transfer between the target proton and the Δ, when plotted in the space of laboratory longitudinal momentum $p_L(\Delta)$ versus the square of the transverse momentum $p_T^2(\Delta)$. We observe that for $|t| = 1$ GeV^2, the maximum value

of $p_L(\Delta)$ is 1.33 GeV/c ($p_T^2(\Delta) = 0$). Then the proton resulting from Δ decay would have laboratory momenta of 1.37 and 0.71 GeV/c corresponding to the decay angles $\theta = 0^\circ$ and $\theta = 180^\circ$, respectively. The identification criterion for protons thus allows essentially full acceptance of Δ's for $|t|$ less than 1 GeV^2. In the following, we impose this t - cut for our study of the Δ^{++} production process.

III. Inclusive and Semi-inclusive Δ^{++} Production Cross Sections

In Fig. 2a,c, we show the effective-mass distributions of the π^+p system, $M(\pi^+p)$, for 100, 200 and 360 GeV/c data, respectively, requiring $|t_{pM}| \leq 1$ GeV^2, where t_{pM} is the square of the four momentum transfer between the incident proton and $M(\pi^+p)$ system. The solid curves represent fits to the data in the region 1.1 GeV $\leq M(\pi^+p) \leq$ 1.6 GeV using a p-wave Breit-Wigner form and a polynomial background (dashed line),

$$\frac{d\sigma}{dM} = a(B.W.) + \sum_i b_i (M - M_{th})^i, \qquad i = 1, 2 \qquad (2)$$

where $$B.W. = \frac{M_o \Gamma}{(M^2 - M_o^2)^2 + M^2\Gamma^2} \quad \text{and} \quad \Gamma = \Gamma_o (q/q_o)^3.$$

M_{th} is the minimum possible π^+p mass. M_o and Γ are the mass and mass-dependent width of the Δ^{++} and q is the momentum of one of the decay products in the Δ rest frame. In the final fits M_o and Γ_o have been fixed at 1220 MeV and 122 MeV respectively. We obtain inclusive Δ^{++} production cross sections of 1.52 ± 0.15, 1.45 ± 0.12, and 1.56 ± 0.10 mb for $|t| \leq 1$ GeV^2 at 100, 200 and 360 GeV/c, respectively[5].

The same fitting procedure has been used to determine semi-inclusive Δ^{++} production cross sections at fixed charge multiplicity n. In Fig. 3 are shown,

for example, distributions of $M(\pi^+p)$ for $n = 4, 6, 8$ and 10 at 360 GeV/c together with fitted curves and background distributions. The fitted cross sections for both inclusive and semi-inclusive Δ^{++} production at all three energies are given in Table I.

Since the ratio of signal to background in the Δ^{++} mass region is relatively large and does not vary too rapidly with n, it is possible to estimate Δ^{++} production cross sections by counting the total number of $p\pi^+$ combinations in a mass slice centered on the Δ^{++} mass. In Table II are shown the numbers of combinations and the corresponding cross sections for the region $1.12 \leq M(\pi^+p) \leq 1.32$ GeV for each charge multiplicity at all three energies. This mass region has been chosen so that comparisons can be made with published results for other reactions[6]. We note that, while the relative amounts of Δ^{++} production estimated in this manner for different multiplicities are roughly consistent with those obtained from our fits, the absolute values of the cross sections obtained using this mass slice tend to be low at the smaller charge multiplicities. In our subsequent studies of the properties of the Δ^{++} system we have used data for all $p\pi^+$ systems in the region ($1.12 < M(p\pi^+) < 1.32$ GeV). The resulting distributions have been scaled to the fitted cross sections of Table I.

In Fig. 4 we have plotted available data for inclusive Δ^{++} production[7] in π^-p interactions as a function of p_{lab} for $16 \text{ GeV/c} \leq p_{lab} \leq 360$ GeV/c. We observe no significant variation of the inclusive Δ^{++} cross section with incident energy over this energy range.

In Fig. 5a are plotted the semi-inclusive Δ^{++} cross sections as a function of n for each of our three energies.[8,9,10] Although the uncertainties

are appreciable, especially at the higher multiplicities, certain systematic trends are observable. The semi-inclusive Δ^{++} cross sections appear to vary with n and with s in a manner qualitatively similar to the variation observed for topological cross sections. As s is increased the distributions of $\sigma_n(\Delta^{++})$ become wider, extending to higher n, and the $\sigma_n(\Delta^{++})$ for the lower multiplicities tend to decrease, leaving the inclusive Δ^{++} cross section approximately unchanged. The value of n for which $\sigma_n(\Delta^{++})$ is largest may tend to move toward larger n, but this cannot be conclusively established with presently available data. To illustrate better the similarities between the $\sigma_n(\Delta^{++})$ distributions and corresponding distributions for topological cross sections, we plot in Fig. 5b the mean number of Δ^{++} per inelastic event, $\langle n_\Delta \rangle = \sigma_n(\Delta^{++})/\sigma_n$, as a function of n. These distributions show much less dependence on n and on s than those of Fig. 5a. $\langle n_\Delta \rangle$ seems roughly independent of s at fixed n. At lower multiplicities $\langle n_\Delta \rangle$ is approximately 0.1 and shows little significant variation with n; at higher multiplicities $\langle n_\Delta \rangle$ seems to decrease from this value. It should be noted, however, that we are limited to $|t| < 1$ GeV^2. If there is appreciable Δ^{++} production at larger $|t|$ in the higher multiplicities it could affect the dependence of $\langle n_\Delta \rangle$ on n. With the limited statistics now available, we can fit our data for $\langle n_\Delta \rangle$ as a function of n for $4 \leq n \leq 14$ at all three energies to the form $\langle n_\Delta \rangle = a + bn$ with $a = 0.12 \pm 0.04$, $b = -0.005 \pm 0.001$.

In Fig. 6, we show mass distributions for the $p\pi^-$ system. No significant signal for $\Delta^0(1232)$ production is observed. Nevertheless, we have fitted these distributions in the same manner described earlier. We obtain Δ^0 production

cross sections of 0.12 ± 0.08, 0.00 ± 0.04, and 0.09 ± 0.03 mb for 100, 200 and 360 GeV/c data, respectively.

IV. Δ^{++} Production Associated with Low-Mass $\Delta^{++}\pi^-$ Systems

Using the high-statistics 360 GeV/c data, we have estimated the amount of Δ^{++} production in which the Δ^{++} comes from the decay of low-mass baryon states. In Fig. 7a, we show the $\Delta^{++}\pi^-$ mass distribution. For comparison we also show the $\Delta^{++}\pi^+$ mass distribution, normalised in the mass region $3 \leq M(\Delta\pi) \leq 5$ GeV. Assuming the $\Delta^{++}\pi^+$ mass distribution as background, it is seen that there is an excess of events in the $\Delta^{++}\pi^-$ mass distribution at low mass, i.e. $M(\Delta^{++}\pi^-) < 2$ GeV. The tables of the Particle Data Group[11] list a number of candidates which may contribute in this mass region. Subtracting the background, we obtain a cross section of 0.53 ± 0.06 mb for this low mass enhancement which presumably can be attributed to the decays $N^* \to \Delta^{++}\pi^-$ in both diffractive and non-diffractive processes. In order to discriminate between contributions from diffractive and non-diffractive processes, we study the production cross section of low-mass $\Delta^{++}\pi^-$ systems as a function of Feynman x. We show x-distributions in Fig. 7b for $\Delta^{++}\pi^-$ and $\Delta^{++}\pi^+$ systems using all events with $M(\Delta\pi) < 2$ GeV. A large peak at $x \approx -1.0$ is observed only for the $\Delta^{++}\pi^-$ system. Using a smooth background in the region of $x < -0.9$, we estimate the cross section for diffractive production of low mass $\Delta^{++}\pi^-$ systems to be ~ 0.12 ± 0.02 mb.

In Fig. 8, we show x distributions for low-mass ($M(\Delta\pi) < 2$ GeV) $M(\Delta\pi)$ systems for 4, 6, 8 and 10 prong events. It is clear from this figure that diffractive production of low-mass $\Delta^{++}\pi^-$ systems is only important for $n = 4$; the corresponding cross section is 0.10 ± 0.01 mb.

We conclude that no more than about 1/3 of the Δ^{++} produced at this energy can come from the $\Delta^{++}\pi^-$ decay of low-mass N^*'s and no more than ~10% can be the result of diffractively produced low-mass N^* systems. Almost all of this diffractive contribution is confined to 4-prong events.

V. Differential Δ^{++} Production Cross Section; Comparison of Δ^{++} and Proton Production

A. Inclusive Cross Sections

We now discuss the invariant differential cross section

$$f(x, p_T^2) \equiv \frac{1}{\pi}\frac{E^*}{\sqrt{s}} \frac{d^2\sigma}{dx dp_T^2} \qquad (3)$$

for inclusive Δ^{++} production. Here x is defined as $x = 2p_L^*/\sqrt{s}$ ($\sqrt{s}$ = total c.m. energy). E^* and p_L^* are the c.m. energy and longitudinal momenta of the Δ and p_T is its transverse momentum. In Fig. 9a, we show the quantity $F(x) = \int f(x, p_T^2) dp_T^2$ as a function of x for the 100, 200 and 360 GeV/c data. The x-distribution shows little dependence, if any, on incident energy.

In Fig. 9b we plot $d\sigma/dp_T^2$ as a function of p_T^2 for Δ^{++} production. This distribution is independent of incident energy. We have fitted these distributions for $p_T^2 < 0.7$ (GeV/c)^2 to the form,

$$d\sigma/dp_T^2 = a \exp(b\, p_T^2 + c\, p_T^4). \qquad (4)$$

The fitted parameters for each energy are given in Table III.

In Fig. 10, we show $F(x)$ for protons produced in 100, 200 and 360 GeV/c π^-p interactions. Here we show the x-distributions (a) for all protons, (b) for protons not associated with Δ^{++}, and (c) for protons exclusively from Δ^{++}. None of these distributions show any significant dependence on incident energy over this energy range.

It is of interest to compare Δ^{++} inclusive distributions with those for protons not associated with the Δ^{++}. In Fig. 9 we have already shown the x- and p_T^2-distributions for Δ^{++}. We now present in Fig. 11 the x- and p_T^2-distributions for protons not associated with Δ^{++}. The most distinctive difference in the single-particle Δ^{++} and proton spectra is observed in the function F(x) (see Figs. 9a and 11a) for $x \leq -0.9$. In this region the proton distribution rises sharply as $x \to -1.0$. This rise is not due to elastic events; they have been removed from the samples. In contrast, the Δ^{++} distribution decreases as $x \to -1.0$. The sharp rise of the cross section for proton production at $x = -1.0$ can be attributed primarily to Pomeron exchange in inelastic reactions. For Δ^{++} production, direct Pomeron exchange is not allowed and hence the suppression of Δ^{++} production near $x = -1.0$ is expected.

B. Semi-Inclusive Δ^{++} Cross Sections

We have also compared single-particle distributions (x- and p_T^2-distributions) for Δ^{++} produced in low- and high-multiplicity events. Since the p_T^2-distributions do not show appreciable changes as a function of prong number or as a function of incident energy, these distributions are not presented. The x-distributions show a dependence on charge multiplicity n but are approximately independent of energy for fixed n.

In Figs. 12a-c we show F(x) for 4-prong, 6-prong, and (8 + 10)-prong events at 360 GeV/c. Production of Δ^{++} is observed over a wider range of x as n increases; also the distribution shifts toward smaller values of $|x|$ with increasing n. We also show F(x) after excluding those Δ^{++} associated with $\Delta^{++}\pi^-$ systems having $x(\Delta^{++}\pi^-) < -0.95$. (As shown in Section IV this should

then remove any effects associated with diffractive N^* production.) We observe that the overall behavior of the x-distribution is basically unchanged aside from the expected reduction in cross section for $n = 4$ events. The dependence of F(x) on n is not determined by N^* production even at low n.

VI. Evidence of Δ^{++} Production Via One-Pion-Exchange

A. Momentum Transfer Distribution and Δ^{++} Density Matrix Elements

Gotsman[12] has pointed out that in an OPEA (one-pion-exchange model with absorption effects folded in) a forward peak should be observed in distributions of $d\sigma/dp_T^2$ or $d\sigma/dt'$, where $t' = t - t_{min}$ (t_{min} = minimum value of the momentum transfer). In Fig. 13 we plot the $d\sigma/dt'$ distribution and fit it (in the range $t' \leq 0.7$ GeV^2) to a form $d\sigma/dt' = A\exp(Bt' + Ct'^2)$. The parameters are listed in Table III. The steepness of this distribution at small t', and also that for the $d\sigma/dp_T^2$ distribution for Δ's (Fig. 9b), are consistent with a one-pion-exchange model including absorption.

Much clearer evidence for OPEA model, however, can be seen in the Δ^{++} decay density matrix elements. Using the method of moments we have determined the matrix elements ρ_{33}, $\mathrm{Re}\,\rho_{31}$ and $\mathrm{Re}\,\rho_{3-1}$ from the angular distributions of $\Delta^{++} \to p\pi^+$ decay. The explicit form of the decay angular function $W(\theta, \phi)$ in terms of these matrix elements can be found in Ref. 1. The density matrix elements are listed in Table IV as a function of energy. All three elements show little or no energy dependence. Because no clear energy dependence is observed for Δ^{++} production as a function of the momentum transfer t' or any other related variable, we have combined data at all three energies. For this high statistics sample we obtain $\rho_{33} = 0.13 \pm 0.01$, $\mathrm{Re}\,\rho_{31} = 0.07 \pm 0.01$ and $\mathrm{Re}\,\rho_{3-1} = 0.01 \pm 0.01$, when integrated over all $|t| < 1$ GeV^2. This

result, together with the separate results for each energy are in good agreement with the predictions[12] of OPEA (given in Table IV) for Δ^{++} production.

In order to estimate the extent to which the values of the matrix elements may be affected by background effects, and to test the sensitivity of this method, we have determined the density matrix elements for $\pi^- p$ systems for $1.12 < M(\pi^- p) < 1.32$ GeV (Δ^0 region). Since we observe no signal in the Δ^0 region, this allows us to estimate the effects of the background under the Δ^{++} (see Table IV). The matrix elements for Δ^{++} production cannot be accounted for by a background effect.

We have also computed matrix elements for the combined sample as a function of $|t|$ (Table V). We observe a significant dependence of ρ_{33} and $\mathrm{Re}\,\rho_{31}$ on t, both of which increase with increasing $|t|$. This is again consistent with what is expected from OPEA.[13]

B. Inclusive Δ^{++} Production and Triple-Regge Analysis

Theoretical calculations[14] for high energy Δ^{++} production in terms of the triple-Regge exchange process have been made. For this purpose, the variables used are t and M_x^2, where M_x is the mass recoiling against the Δ^{++}. The invariant cross section $f(x, p_T^2)$ of equation (3) can be re-expressed in terms of these variables as

$$f(x, p_T^2) = \frac{d^2\sigma}{dt \; d(M_x^2/s)},$$

where s is the square of the total center of mass energy.

In terms of a triple-Regge model, the process of Δ^{++} production should be described by the diagram in Fig. 14, and the cross section should be given by

$$\frac{d^2\sigma}{dt\, d(M_x^2/s)} = G_{ijk} (M_x^2/s)^{[\alpha_k(0) - \alpha_i(t) - \alpha_j(t)]} s^{[\alpha_k(0) - 1]} \qquad (5)$$

Here i, j, k refer to the Regge trajectories, and G_{ijk} is the combined triple-Regge coupling constant obtained by multiplying the individual couplings. The subscript k corresponds to the Regge trajectory coupling the incident and outgoing beam particle while i and j correspond to the Regge trajectory connecting the target proton and outgoing Δ^{++}.

In Fig. 15a, we show the t-distribution of Δ^{++} production for 100, 200 and 360 GeV/c. This distribution is independent of incident energy. In Fig. 15b, we show cross sections as a function of M_x^2/s for the three energies for $|t| \leq 1$ GeV^2. It can be seen from eqn. (5) that for fixed t and M_x^2/s, the invariant cross section $d^2\sigma/dt\, d(M_x^2/s)$ is proportional to $s^{\alpha_k(0) - 1}$. The lack of significant energy dependence of the invariant cross section as observed in Fig. 15 thus requires $\alpha_k(0) \approx 1.0$. We have also investigated the s-dependence of the invariant cross section, eqn. (5), for different t and M_x^2/s intervals (see Fig. 16). We find that the invariant cross section is independent of s and thus $\alpha_k(0)$ is consistent with 1; therefore the $\pi^-\pi^-$ vertex is consistent with the exchange of the Pomeron trjaectory ($\alpha_k(0) = 1$).

We now attempt to find the parameters for the trajectory associated with the p-Δ vertex. Setting $\alpha_k(0) = 1$, and assuming $\alpha_i(t) = \alpha_j(t) = \alpha(t)$, the invariant cross section, Eqn. (5), now becomes

$$\frac{d^2\sigma}{dt\, d\, M_x^2/s} \propto (M_x^2/s)^{1 - 2\alpha(t)}. \qquad (6)$$

Since the invariant cross section is found to be energy independent, we have combined the 100, 200 and 360 GeV/c data to improve our statistics (~3,000

events in the Δ^{++} mass range) in order to obtain a more accurate value of $\alpha(t)$. For fixed t we have studied the invariant cross section as a function of M_x^2/s. These distributions are fitted with expression (6) to determine $\alpha(t)$. In Figure 17, we show a few of these distributions. The resultant values of $\alpha(t)$ are plotted in Figure 18. We observe that as $t \to 0$, $\alpha(0) \to 0$, consistent with the intercept expected for the pion trajectory. This trajectory, as constructed by Moriarty[15], is also shown (dashed curve) in Fig. 18. We conclude that the one-pion-exchange diagram is dominant in the region (small t, small M_x^2/s) where triple-Regge analysis is valid.

C. The Recoil System

Another approach to the study of the exchange processes involved in Δ^{++} production is to analyse properties of the system recoiling from the Δ^{++}. In an OPE model we should be able to factor the reaction $\pi^- p \to \Delta^{++} X^{--}$ into two virtual processes, $pE^+ \to \Delta^{++}$ and $\pi^- E^+ \to X^{--}$, where E is the exchange particle. Studying features of the mass recoiling from the Δ would then be equivalent to studying the virtual 2-pion scattering process $\pi^-\pi^- \to X^{--}$ if the exchange particle is a pion. We might then expect the recoil system to exhibit at least some of the properties observed in real 2-body scattering.

In Fig. 19a, we show the average multiplicity $< m >$ of the charged particles in the recoil system as a function of M_x^2 for each energy. The moment $< m(m-1) >$ is plotted in Fig. 19b. We observe that both $< m >$ and $< m(m-1) >$ are independent of incident energy[1,16]. Using real $\pi^- p$ scattering data Whitmore[16] has found that the mean charge multiplicity $< n >$ and the moment $< n(n-1) >$ can be parametrized as $< n > = A + B \ln s + C \ln^2 s$.

Using Whitmore's parameters we calculate $< m >$ and $< m(m-1) >$ for the virtual scattering process as a function of M_x^2 as shown in Fig. 19a and Fig. 19b. The good agreement between these curves and the data as a function of M_x^2 provides further support for the supposition that we are observing a process similar to two-body scattering.

VII. Summary and Conclusions

We have determined the $\Delta^{++}(1232)$ production cross sections for $\pi^- p$ interactions at 100, 200 and 360 GeV/c. The inclusive cross sections are found to be essentially energy independent in the Fermilab energy range. We find that no more than 1/3 of the Δ^{++} produced can be the result of the decay of low-mass $\Delta^{++}\pi^-$ systems, and less than 10% of the cross section can be attributed to diffractively produced N^* states. Almost all of this diffractive contribution is confined to 4-prong events. Moments analyses have been performed to determine the spin density matrix elements for Δ^{++} as a function of the momentum transfer t. We find that the values of the matrix elements are in good agreement with the predictions of a model of one-pion-exchange with absorption (OPEA) for the Δ^{++} production process. The observed trend for the individual density matrix elements to increase as the magnitude of the momentum transfer increases is also in accord with expected OPEA behavior. A triple-Regge analysis has been carried out to study the Δ^{++} recoil system. Results of this study again are consistent with Reggeized one-pion-exchange.

Acknowledgements

We would like to thank the Fermilab 30" bubble chamber crew for their

aid in performing this experiment. Special thanks go to the scanning and measuring staff and the staffs of all our institutions for an outstanding effort.

References

1. N. N. Biswas et al., Phys. Rev. D16, 2090 (1977).
2. H. L. Price, Technical Report No. 77-014, P. P. No. 77-032. Thesis, University of Maryland, August (1976).
3. N. N. Biswas et al., Phys. Rev. Lett. 35, 1059 (1975); E. D. Fokitis Ph. D. thesis, University of Notre Dame, (unpublished).
4. G. A. Smith in Particles and Fields, 1973, Proceedings of the Berkeley APS Meeting, edited by H. Bingham et al. (AIP, New York, 1974).
5. In reference 1 the $\Delta^{++}(1232)$ cross section was determined using a simple, unconstrained Breit-Wigner and a quadratic background. This resulted in cross sections that were generally 10 - 20% lower than those found using the current method.
6. For example see S. J. Barish et al., Phys. Rev. D12, 1260 (1975); D. Brick et al., in Proceedings of the XVIII International Conference on High Energy Physics, Tbilisi (1976), and references cited therein.
7. The 16 GeV/c $\nu^- p$ data is from the ABBCCHLVW Collaboration in Proceedings of the XVIII International Conference on High Energy Physics, Tbilisi (1976).
8. E. L. Berger et al., Nucl. Phys. B77, 365 (1974).
9. D. Ljung et al., Phys. Rev. D15, 3163 (1977).
10. A. Firestone et al., Phys. Rev. D14, 2902 (1976).
11. T. G. Trippe et al., Rev. Mod. Phys. 48, 1 (1976).
12. E. Gotsman, Phys. Rev. D9, 1575 (1974).
13. N. N. Biswas et al., Phys. Rev. D9, 2705 (1970).
14. See for example, R. D. Field and G. C. Fox, Nucl. Phys. B80, 367 (1974); S. N. Ganguli and B. Sadoulet, Nucl. Phys. B53, 458 (1973).
15. K. J. M. Moriarty et al., Phys. Rev. D16, 130 (1977).
16. J. Whitmore, Phys. Rep. 27C, 187 (1976).

TABLE I.

FITTED Δ^{++} PRODUCTION CROSS SECTIONS

n	Cross Sections (mb) for $\lvert t \rvert < 1$ GeV^2 at P_{lab} = 100 GeV/c	200 GeV/c	360 GeV/c
4	0.40 ± .05	0.24 ± .04	0.31 ± .03
6	0.55 ± .06	0.35 ± .04	0.37 ± .04
8	0.30 ± .07	0.37 ± .05	0.36 ± .04
10	0.12 ± .05	0.33 ± .04	0.24 ± .04
12	0.04 ± .05	0.12 ± .04	0.13 ± .03
≥ 14	---	0.02 ± .01	0.08 ± .03
Total	1.52 ± .15	1.45 ± .12	1.56 ± .10

TABLE II.

CROSS SECTIONS FOR $\lvert t \rvert < 1$ GeV^2

AND $1.12 < M(p\pi^+) < 1.32$ GeV

Multiplicity	100 GeV/c Events	100 GeV/c σ (mb)	200 GeV/c Events	200 GeV/c σ (mb)	360 GeV/c Events	360 GeV/c σ (mb)
4	149	0.30 ± .02	166	0.20 ± .02	302	0.23 ± .01
6	206	0.41 ± .03	219	0.27 ± .02	335	0.27 ± .01
8	57	0.31 ± .04	176	0.27 ± .02	335	0.28 ± .02
10	20	0.11 ± .02	146	0.23 ± .02	233	0.20 ± .01
12	9	0.06 ± .02	51	0.09 ± .01	148	0.14 ± .01
14	1	0.0 ± .01	18	0.03 ± .01	70	0.07 ± .01
≥ 16			11	0.02 ± .01	58	0.06 ± .02
Sum	442	1.20 ± .06	792	1.11 ± .04	1481	1.25 ± .03

Table III. Fitted Parameters for $d\sigma/dp_T^2 = a \exp(bp_T^2 + cp_T^4)$ and for $d\sigma/dt' = A \exp(Bt' + Ct'^2)$

Parameters		P_{lab} = 100 GeV/c	P_{lab} = 200 GeV/c	P_{lab} = 360 GeV/c
	a (mb/(GeV/c)^2)	9.62 ± 0.95	8.91 ± 0.64	9.80 ± 0.48
p_T^2	b (GeV/c)$^{-2}$	-9.79 ± 1.24	-7.49 ± 0.88	-7.98 ± 0.56
	c (GeV/c)$^{-4}$	5.75 ± 2.45	1.06 ± 1.83	2.11 ± 1.12
	A (mb/GeV^2)	8.12 ± 0.53	8.30 ± 0.45	7.70 ± 0.51
t'	B (GeV)$^{-2}$	-6.08 ± 0.97	-5.64 ± 0.61	-5.51 ± 0.41
	C (GeV)$^{-4}$	3.96 ± 1.48	3.61 ± 1.10	3.06 ± 0.65

Table IV. Density Matrix Elements of $\Delta^{++}(1232)$ Produced in $\pi^- p$ Reaction

Beam Momentum	$\rho_{3,3}$	$Re\,\rho_{3,1}$	$Re\,\rho_{3,-1}$
100 GeV/c	0.15 ± 0.03	0.01 ± 0.03	-0.02 ± 0.02
200 GeV/c	0.12 ± 0.02	0.07 ± 0.02	0.02 ± 0.02
360 GeV/c	0.13 ± 0.03	0.05 ± 0.02	0.00 ± 0.02
Background ("Δ^{0}" region)	0.06 ± 0.02	0.11 ± 0.02	0.03 ± 0.02
100, 200 and 360 GeV/c combined	0.13 ± 0.01	0.07 ± 0.01	0.01 ± 0.01
Pure OPE	0	0	0
OPE + Absorption	0.12	0.06	0.03

TABLE V.

$|t|$-DEPENDENCE OF THE Δ^{++} DENSITY MATRIX ELEMENTS FOR 100 + 200 + 360 GeV/c $\pi^- p$ DATA COMBINED

$\|t\|$-interval GeV^2	ρ_{33}	Re $\rho_{3,1}$	Re $\rho_{3,-1}$
0.05 - 0.2	0.08 ± .02	0.03 ± .02	-0.02 ± .02
0.2 - 0.4	0.12 ± .01	0.03 ± .02	0.00 ± .02
0.4 - 0.6	0.14 ± .03	0.08 ± .02	0.00 ± .02
0.6 - 1.0	0.18 ± .02	0.10 ± .02	0.03 ± .02

Figure Captions

Fig. 1 Kinematics of Δ^{++} production for $|t_{p\Delta}| = 1$ and 2 GeV^2. The curves define $t_{p\Delta}$ as a function of transverse momentum squared $p_T^2(\Delta)$ and laboratory longitudinal momentum $p_L(\Delta)$.

Fig. 2 Effective mass distributions of the $\pi^+ p$ system produced in $\pi^- p$ interactions at beam momenta of (a) 100 GeV/c, (b) 200 GeV/c and (c) 360 GeV/c.

Fig. 3 Effective mass distributions of the $\pi^+ p$ system produced in 360 GeV/c $\pi^- p$ interactions as a function of charge multiplicity n for (a) n = 4, (b) n = 6, (c) n = 8, and (d) n = 10.

Fig. 4 Inclusive Δ^{++} cross section in $\pi^- p$ interactions as a function of laboratory momentum.

Fig. 5 (a) Topological Δ^{++} cross sections in $\pi^- p$ interactions at 100, 200 and 360 GeV/c.

(b) Average number of Δ^{++} per inelastic event as a function of charge multiplicity n. The curve is a fit to 100 + 200 + 360 GeV/c data combined.

Fig. 6 Effective mass distributions of the $\pi^- p$ system produced in $\pi^- p$ interactions at beam momenta of (a) 100 GeV/c, (b) 200 GeV/c, and (c) 360 GeV/c.

Fig. 7 (a) Effective mass distribution for $\Delta^{++}\pi^-$ systems, and for $\Delta^{++}\pi^+$ systems for 360 GeV/c data. The $\Delta^{++}\pi^+$ distribution has been normalized to the $\Delta^{++}\pi^-$ distribution in the region $3.0 \leq M(\Delta\pi) \leq 5.0$ GeV. (b) Differential cross section $d\sigma/dx$ as a function of x for $\Delta^{++}\pi^-$ and $\Delta^{++}\pi^+$ systems having $M(\Delta\pi) \leq 2.0$ GeV. The $\Delta^{++}\pi^+$ distribution is normalized to the $\Delta^{++}\pi^-$ distribution in the region $x > -0.8$.

Fig. 8 Differential cross sectiond $d\sigma/dx$ for various charge multiplicities n as a function of x for $\Delta^{++}\pi^-$ and $\Delta^{++}\pi^+$ systems having $M(\Delta\pi) < 2$ GeV for (a) $n = 4$, (b) $n = 6$, (c) $n = 8$, and (d) $n = 10$ for 360 GeV/c data. The $\Delta^{++}\pi^+$ distribution is normalised to the $\Delta^{++}\pi^-$ distribution in the region $x > -0.8$.

Fig. 9 (a) Inclusive Δ^{++} production cross section as a function of x for 100, 200 and 360 GeV/c data.
(b) Differential cross section $d\sigma/dp_T^2$ for each energy. The curve is the result of a fit to 360 GeV/c data.

Fig. 10 Invariant cross section F(x) as a function of x for all protons, protons not associated with the Δ^{++}, and protons resulting from Δ^{++} decay.

Fig. 11 (a) Invariant cross section F(x) as a function of x for non-Δ^{++} protons.
(b) Differential cross section $d\sigma/dp_T^2$ as a function of p_T^2 for non-Δ^{++} protons. The curve is a fit to 360 GeV/c data.

Fig. 12 Invariant Δ^{++} production cross section F(x) as a function of x for (a) $n = 4$, (b) $n = 6$, and (c) $n = 8$ and 10 in 360 GeV/c data. Also shown are these distributions after requiring that $x(\Delta^{++}\pi^-)$ be greater than -0.95.

Fig. 13 Differential cross section $d\sigma/dt'$ as a function of t'. The curve is a fit to 360 GeV/c data.

Fig. 14 Triple-Regge diagram for Δ^{++} production.

Fig. 15 (a) Momentum-transfer (squared) distribution $d\sigma/dt$ as a function of $|t|$ for Δ^{++} production in 100, 200 and 360 GeV/c π^-p interactions.

Fig. 15 (b) Differential cross section for the system recoiling from the Δ^{++}, $d\sigma/d(M_x^2/s)$ as a function of M_x^2/s for data at each energy.

Fig. 16 Double differential cross section $d\sigma/dt\,d(M_x^2/s)$ as a function of M_x^2/s for various $|t|$ intervals: $0.1 < |t| < 0.2$, $0.2 < |t| < 0.3$, $0.4 < |t| < 0.5$ and $0.8 < |t| < 0.9$ GeV^2.

Fig. 17 $d\sigma/dt\,d(M_x^2/s)$ as a function of M_x^2/s is shown for the combined 100, 200 and 360 GeV/c data for various $|t|$ intervals: $0.1 < |t| < 0.2$, $0.2 < |t| < 0.3$, $0.3 < |t| < 0.4$ and $0.5 < |t| < 0.6$ GeV^2. The curves are the result of fits to the data (see text).

Fig. 18 Regge trajectory parameters $\alpha(t)$ as a function of t as determined from the present analysis (see text). The curve corresponds to pion trajectory as obtained in ref. 15.

Fig. 19 (a) Average multiplicity $\langle n \rangle$ recoiling from the Δ^{++} as a function of recoil mass-squared M_x^2 for 100, 200 and 360 GeV/c data; and (b) Second moment $\langle n(n-1) \rangle$ as a function of M_x^2. The curves are calculated from the parametrisation of π^-p data (see text and ref. 16).

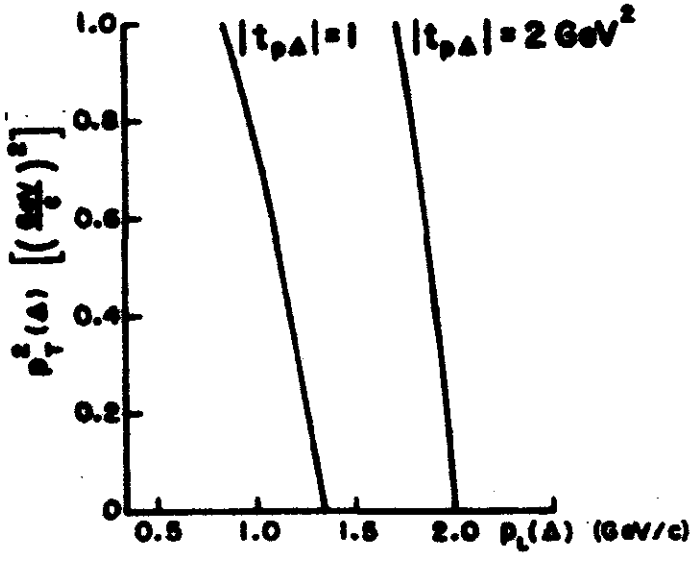
$|t_{p\Delta}|=1$
$|t_{p\Delta}|=2\ GeV^2$
$p_T^2(\Delta)\ [(\frac{d\sigma}{dp_T^2})^{-1}]$
1.0
0.8
0.6
0.4
0.2
0
0.5
1.0
1.5
2.0
$p_L(\Delta)$ (GeV/c)

Fig. 1

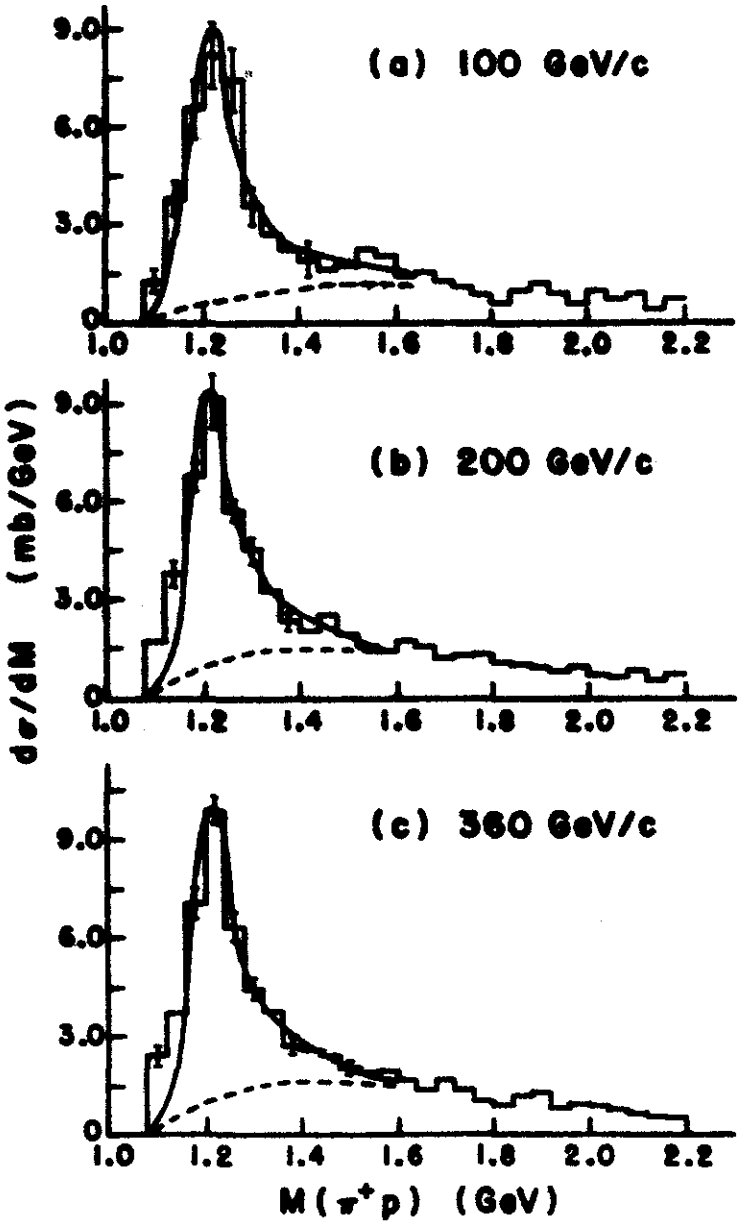
(a) 100 GeV/c
(b) 200 GeV/c
(c) 360 GeV/c
$d\sigma/dM$ (mb/GeV)
9.0
6.0
3.0
0
1.0
1.2
1.4
1.6
1.8
2.0
2.2
M(π^+p) (GeV)

Fig. 2

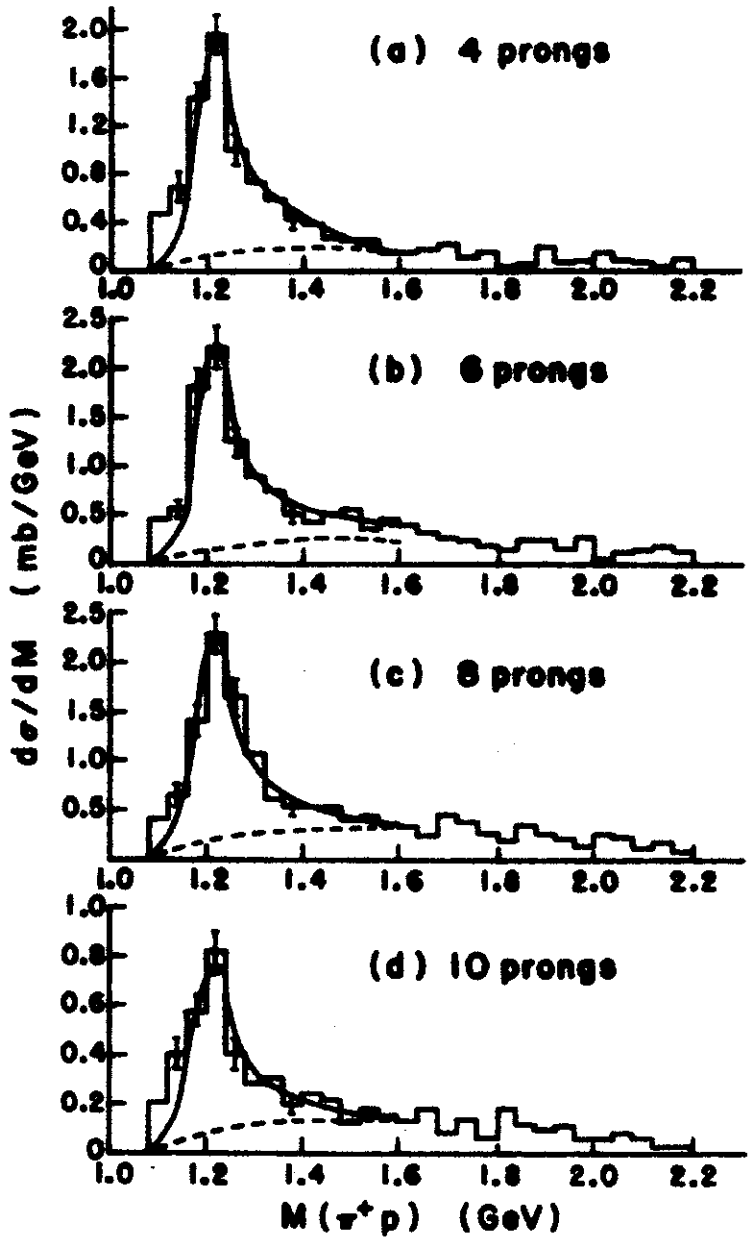
(a) 4 prongs
(b) 6 prongs
(c) 8 prongs
(d) 10 prongs
dσ/dM (mb/GeV)
M(π⁺p) (GeV)

Fig. 3

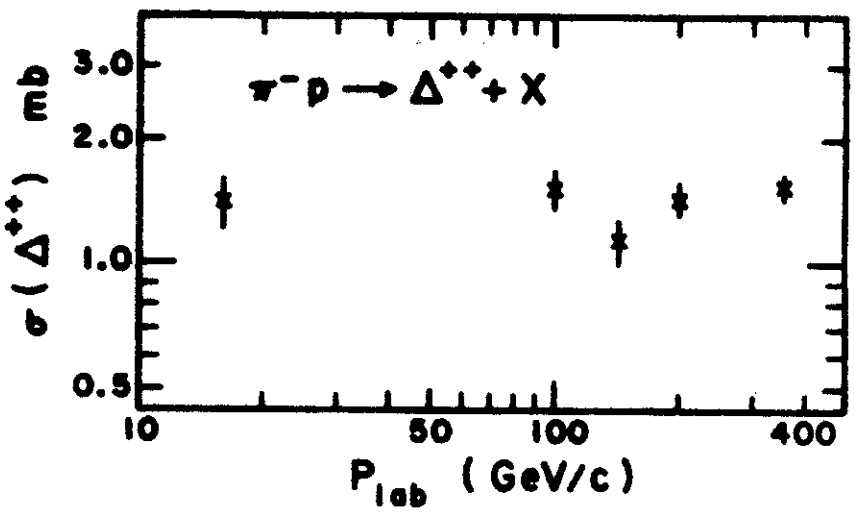
π⁻p → Δ⁺⁺ + X
σ(Δ⁺⁺) mb
P_lab (GeV/c)

Fig. 4

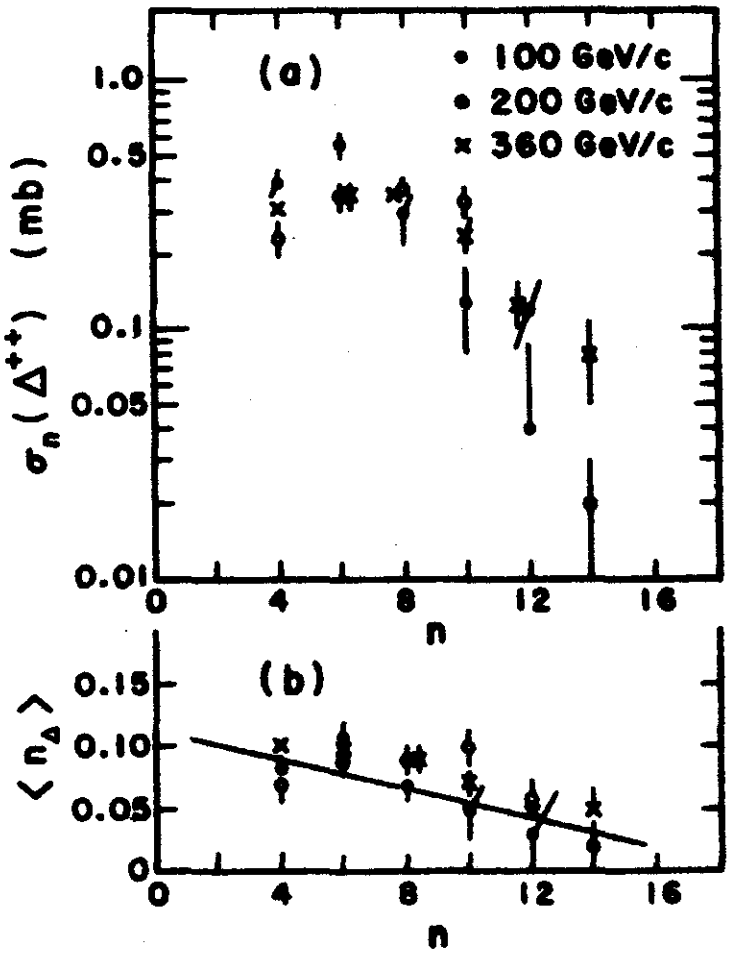
(a)
• 100 GeV/c
• 200 GeV/c
× 360 GeV/c
$\sigma_n(\Delta^{++})$ (mb)
1.0
0.5
0.1
0.05
0.01
0
4
8
12
16
n
(b)
$\langle n_\Delta \rangle$
0.15
0.10
0.05
0
0
4
8
12
16
n

Fig. 5

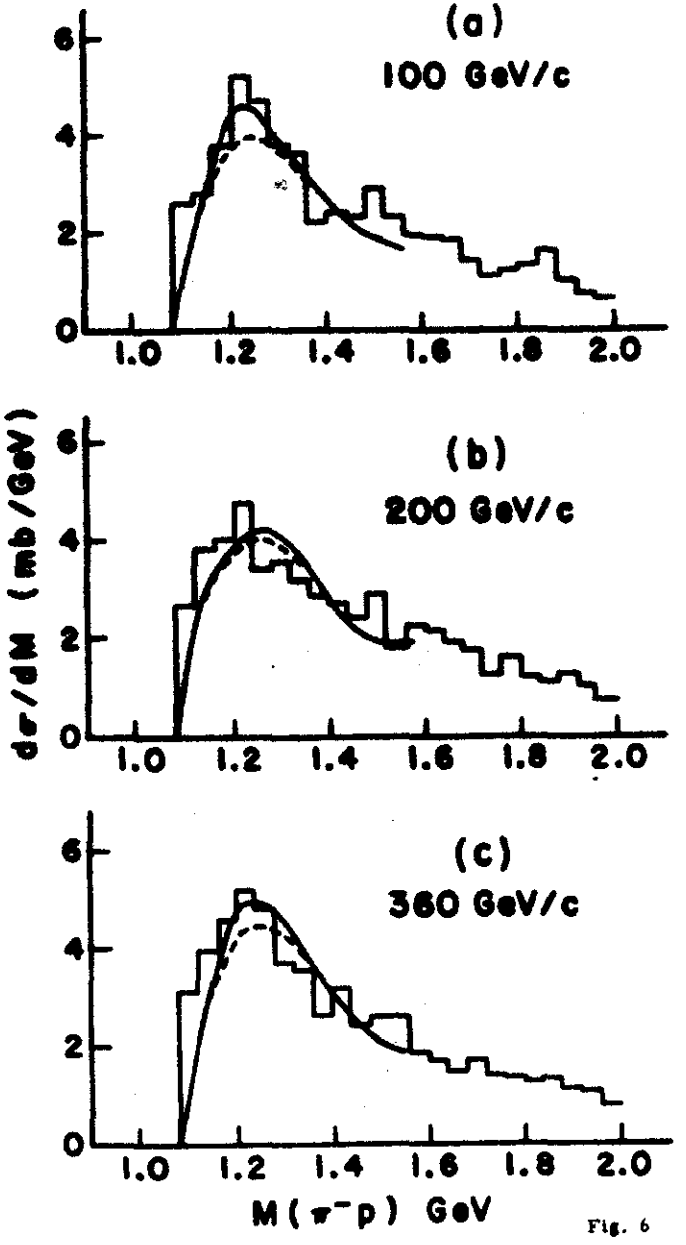
(a)
100 GeV/c
(b)
200 GeV/c
(c)
360 GeV/c
dσ/dM (mb/GeV)
6
4
2
0
1.0
1.2
1.4
1.6
1.8
2.0
M(π⁻p) GeV

Fig. 6

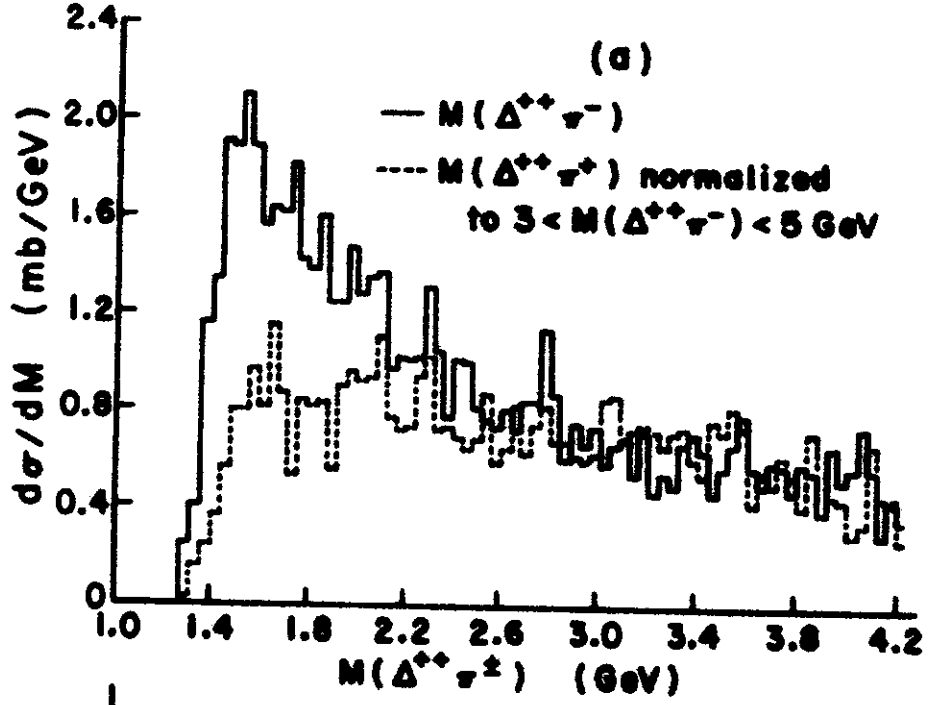
(a)
— M(Δ++π−)
---- M(Δ++π+) normalized
to 3 < M(Δ++π−) < 5 GeV
dσ/dM (mb/GeV)
M(Δ++π±) (GeV)

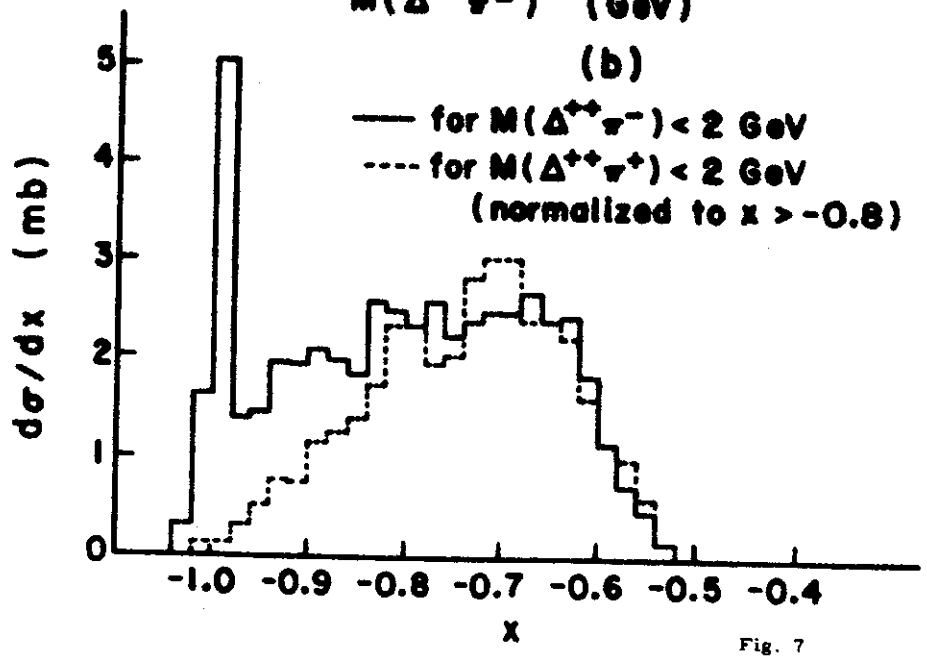
(b)
— for M(Δ++π−) < 2 GeV
---- for M(Δ++π+) < 2 GeV
(normalized to x > −0.8)
dσ/dx (mb)
X

Fig. 7

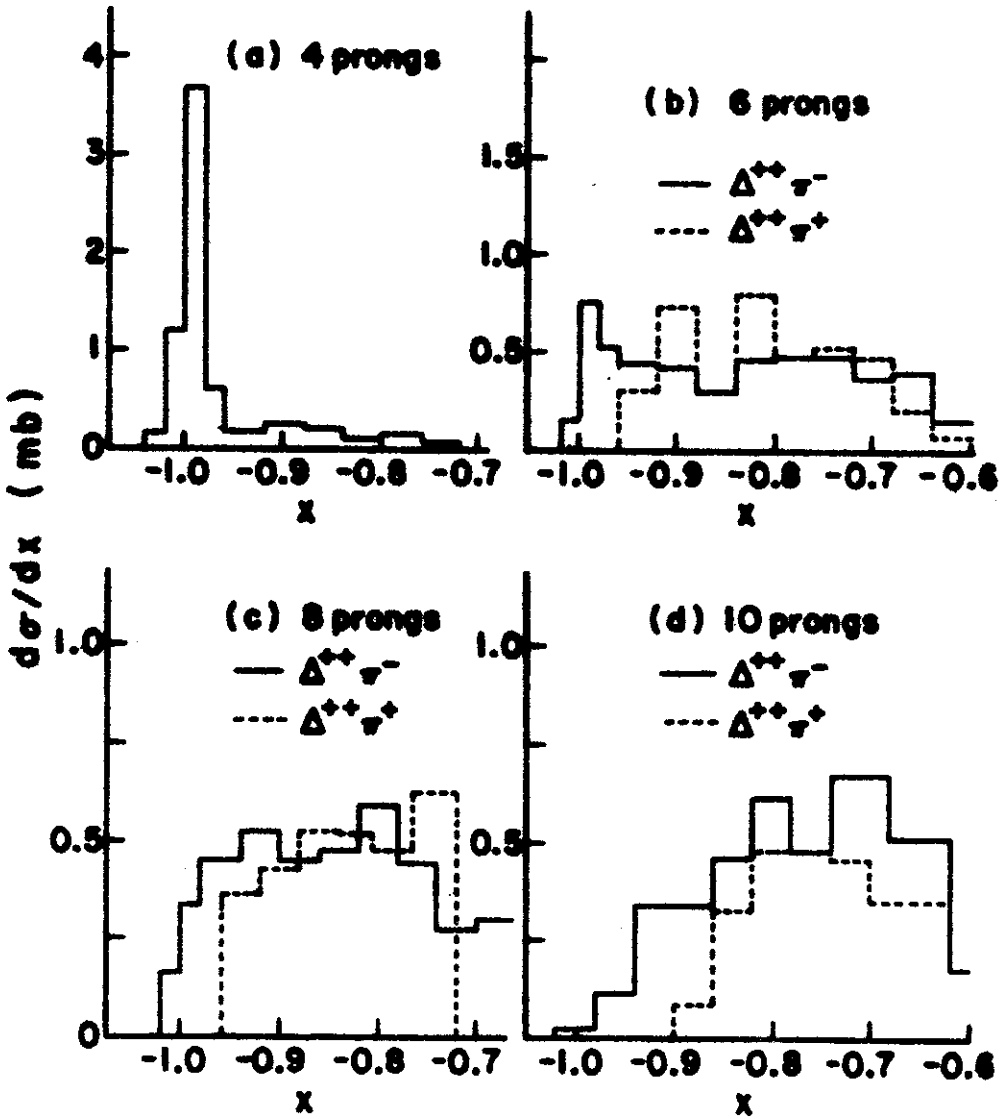
(a) 4 prongs
(b) 6 prongs
(c) 8 prongs
(d) 10 prongs
— Δ++π−
---- Δ++π+
dσ/dx (mb)
X

Fig. 8

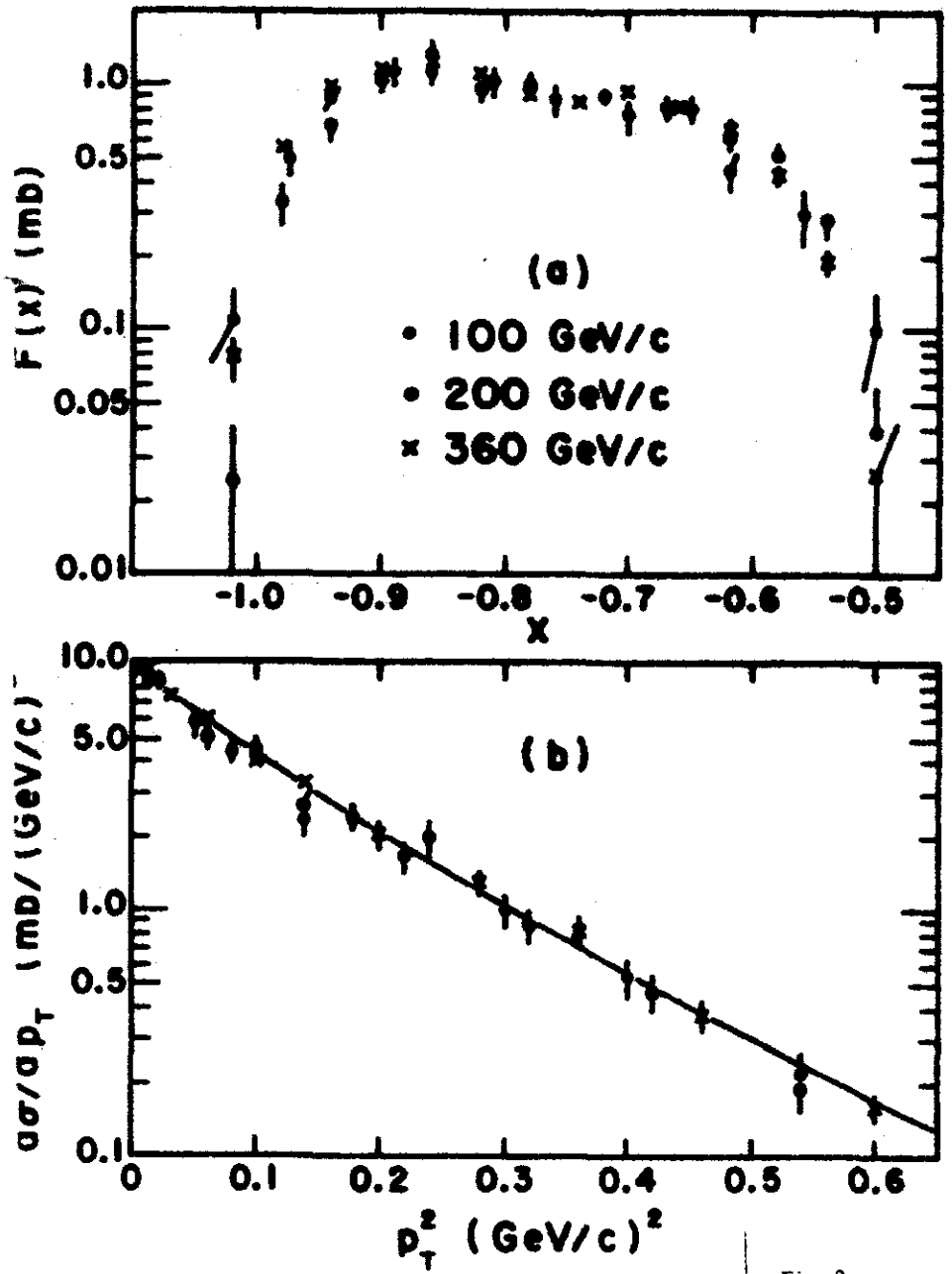
(a)
• 100 GeV/c
• 200 GeV/c
× 360 GeV/c
F(x) (mb)
X
(b)
$d\sigma/dp_T$ (mb/(GeV/c))
p_T^2 (GeV/c)^2

Fig. 9

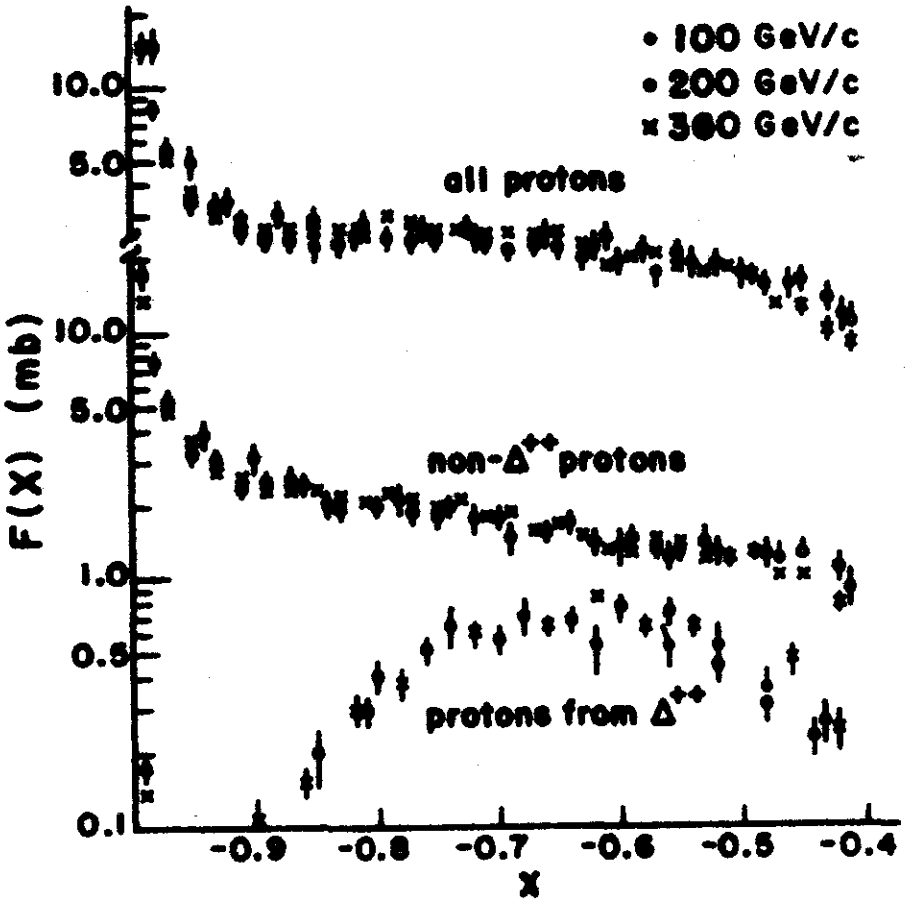
• 100 GeV/c
• 200 GeV/c
× 360 GeV/c
all protons
non-Δ^{++} protons
protons from Δ^{++}
F(X) (mb)
X

Fig. 10

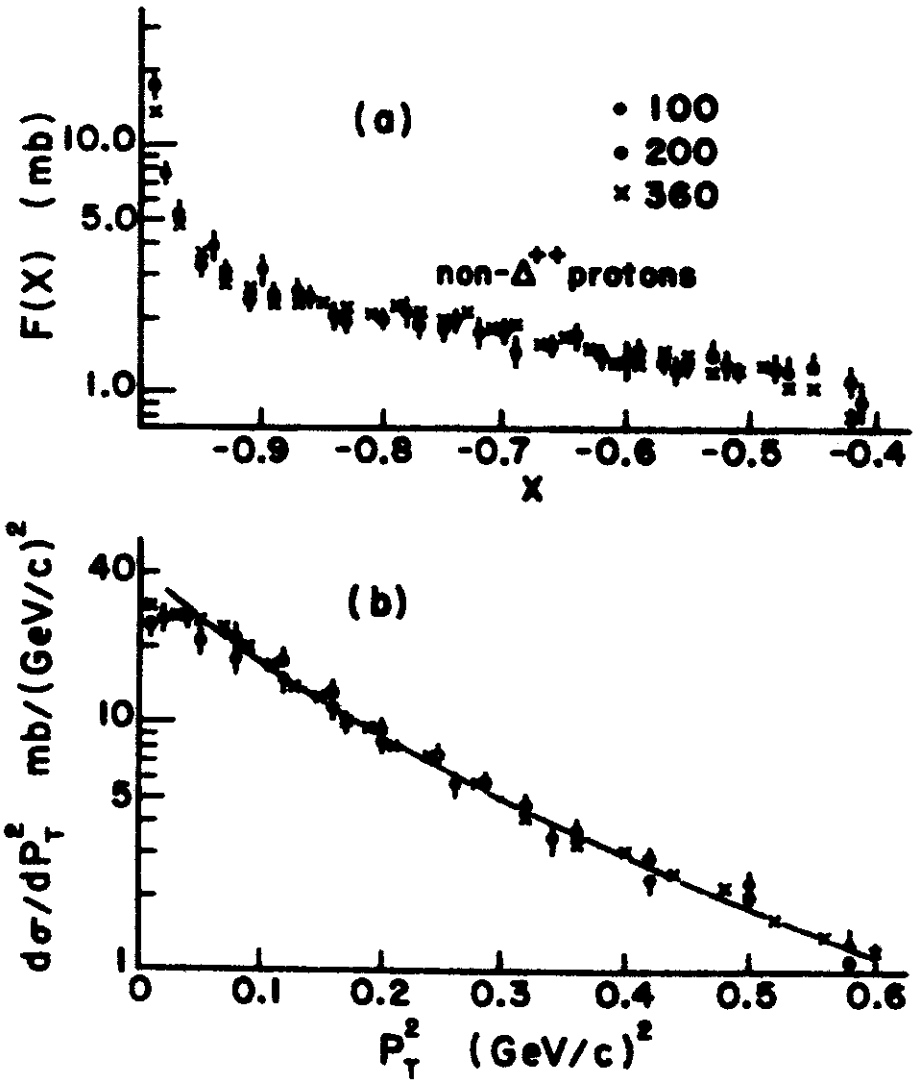
(a)
• 100
• 200
× 360
non-Δ++ protons
F(X) (mb)
10.0
5.0
1.0
-0.9
-0.8
-0.7
-0.6
-0.5
-0.4
X
(b)
dσ/dP²T mb/(GeV/c)²
40
10
5
1
0
0.1
0.2
0.3
0.4
0.5
0.6
P²T (GeV/c)²

Fig. 11

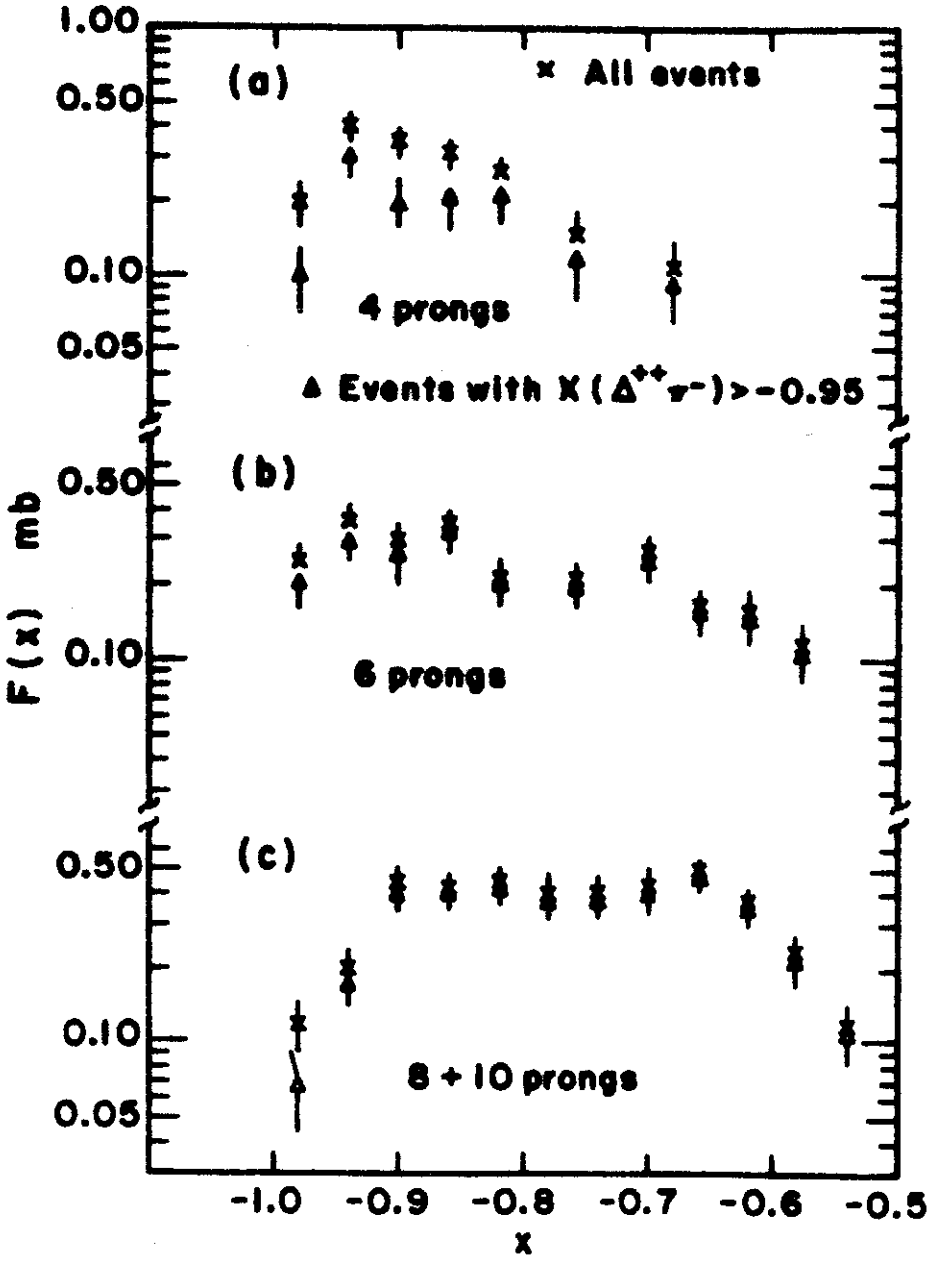
(a)
× All events
4 prongs
▲ Events with X(Δ++π−)>−0.95
(b)
6 prongs
(c)
8 + 10 prongs
F(x) mb
1.00
0.50
0.10
0.05
0.50
0.10
0.50
0.10
0.05
-1.0
-0.9
-0.8
-0.7
-0.6
-0.5
X

Fig. 12

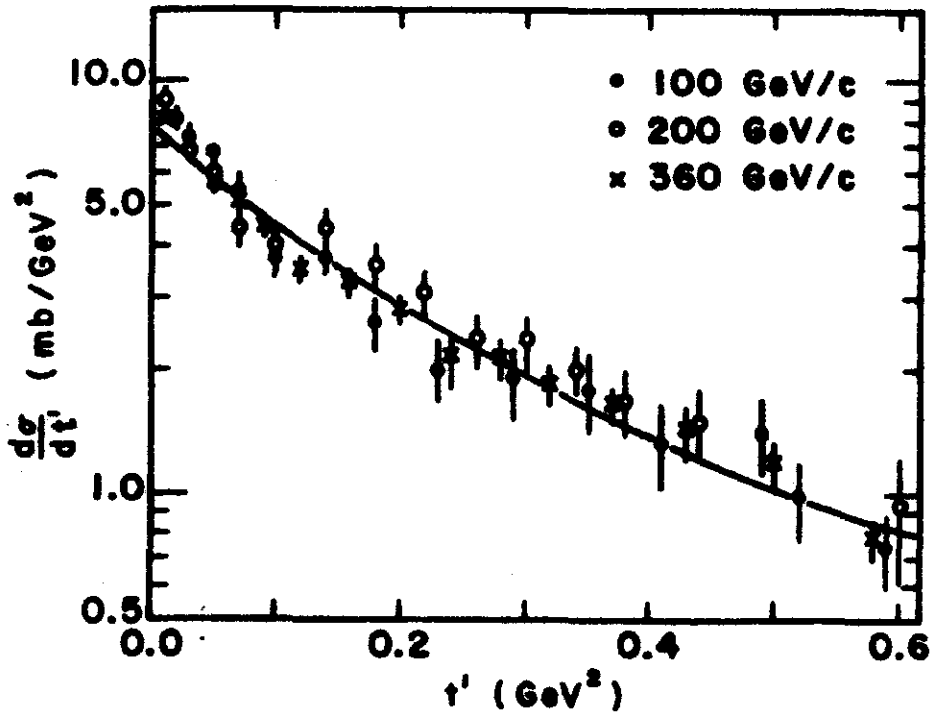
• 100 GeV/c
∘ 200 GeV/c
× 360 GeV/c
10.0
5.0
1.0
0.5
0.0
0.2
0.4
0.6
dσ/dt' (mb/GeV²)
t' (GeV²)

Fig. 13

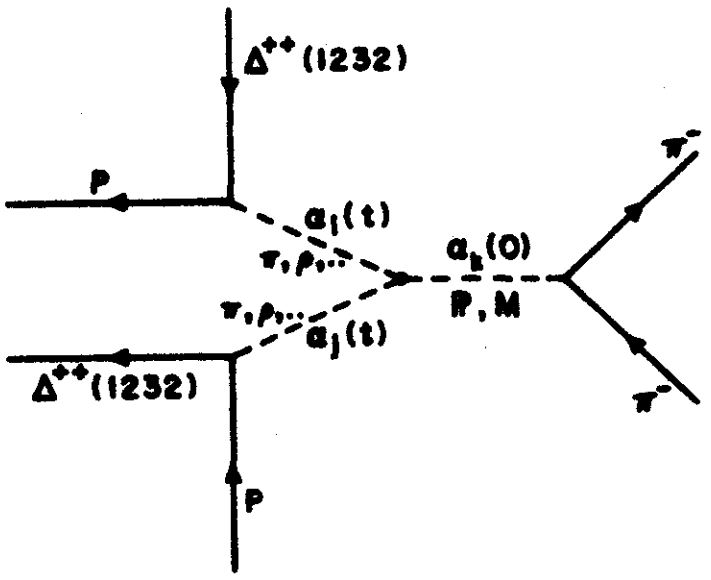
Δ⁺⁺(1232)
P
α_j(t)
π, ρ, ...
α_k(0)
P, M
π, ρ, ...
α_j(t)
Δ⁺⁺(1232)
P
π⁻
π⁻

Fig. 14

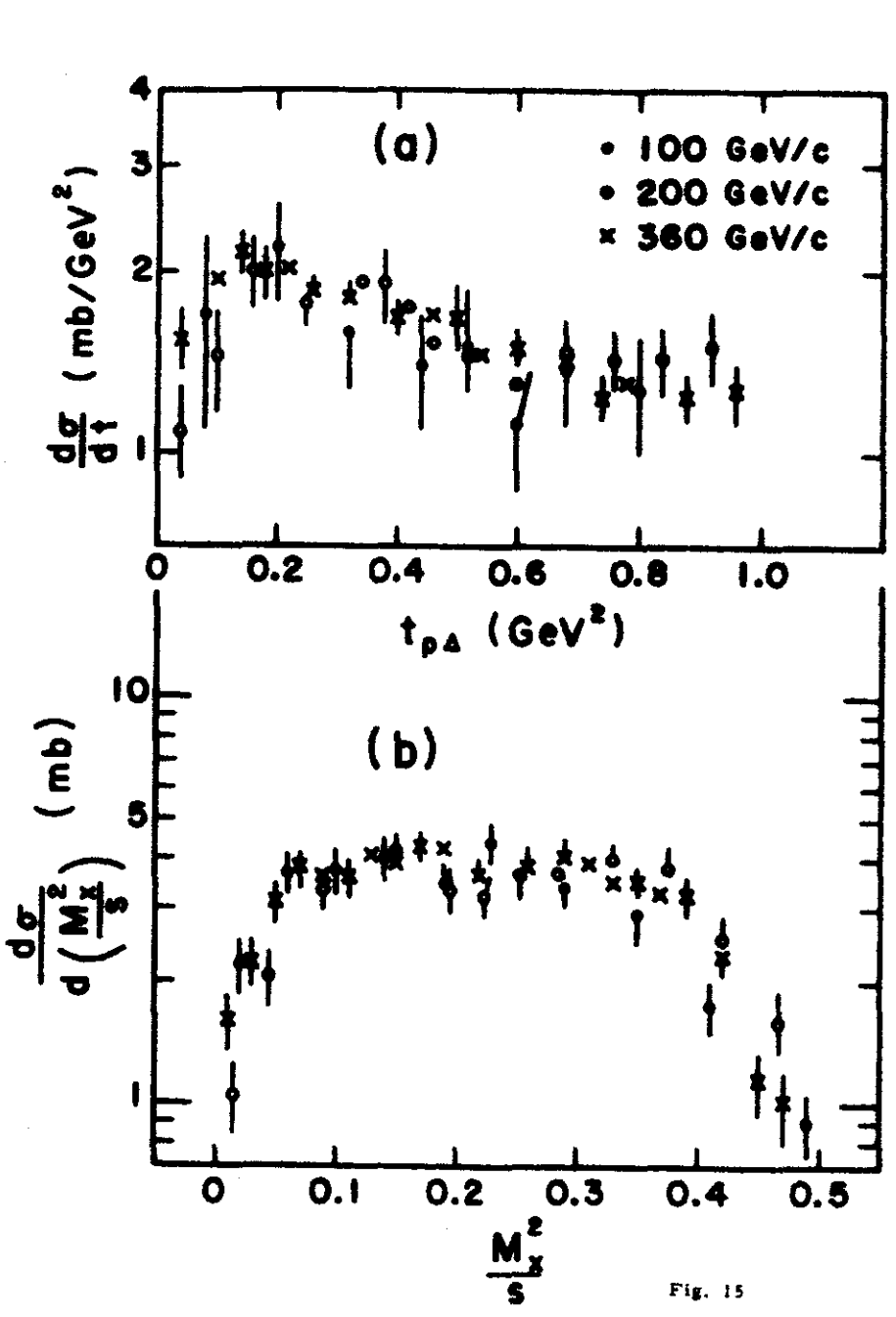
(a)
• 100 GeV/c
• 200 GeV/c
× 360 GeV/c
$\frac{d\sigma}{dt}$ (mb/GeV^2)
$t_{p\Delta}$ (GeV^2)
(b)
$\frac{d\sigma}{d\left(\frac{M_x^2}{s}\right)}$ (mb)
$\frac{M_x^2}{s}$

Fig. 15

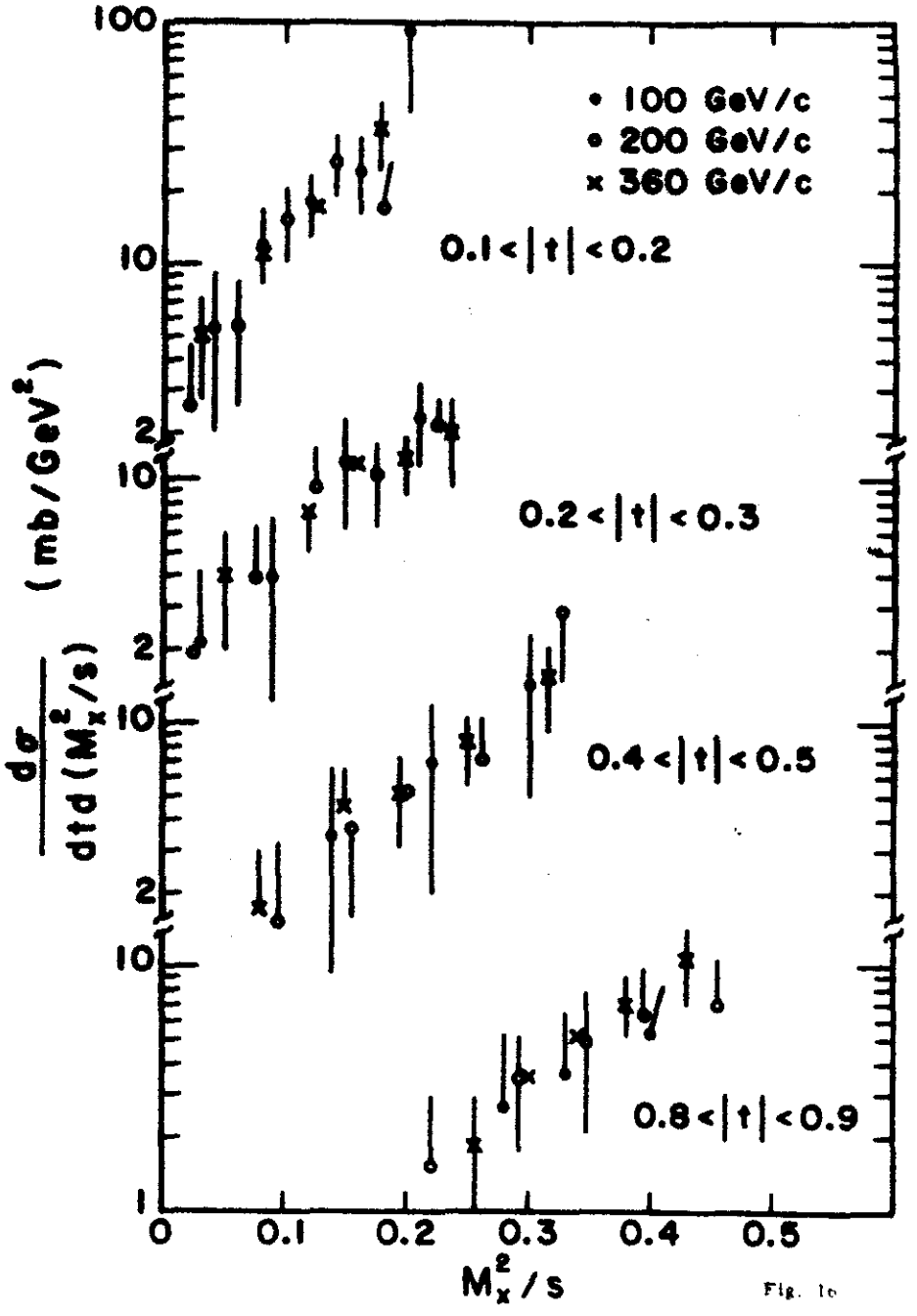
• 100 GeV/c
• 200 GeV/c
× 360 GeV/c
0.1 < |t| < 0.2
0.2 < |t| < 0.3
0.4 < |t| < 0.5
0.8 < |t| < 0.9
$\frac{d\sigma}{dt\,d(M_x^2/s)}$ (mb/GeV^2)
M_x^2/s

Fig. 16

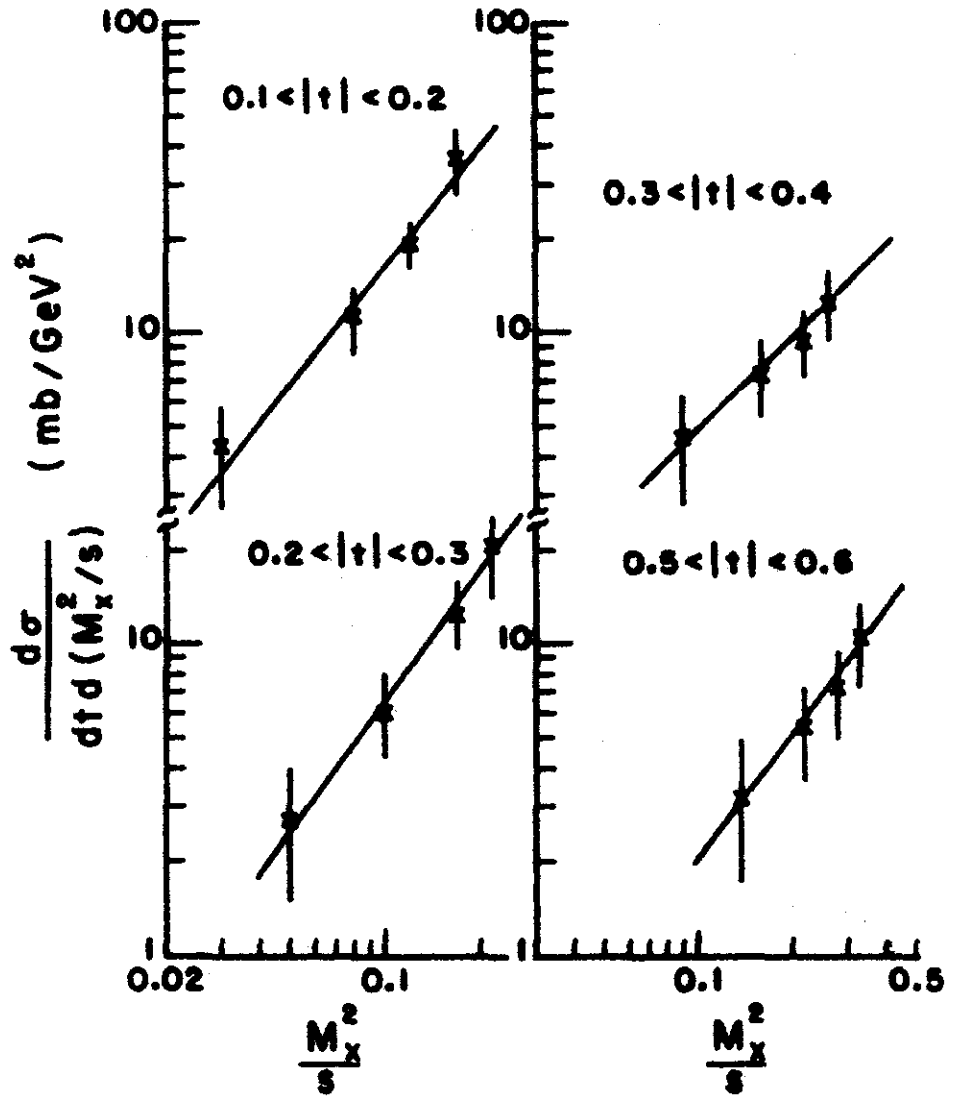
100
10
1
0.1<|t|<0.2
0.3<|t|<0.4
0.2<|t|<0.3
0.5<|t|<0.6
0.02
0.1
0.5
$\frac{d\sigma}{dt\,d(M_X^2/s)}$ (mb/GeV^2)
$\frac{M_X^2}{s}$

Fig. 17

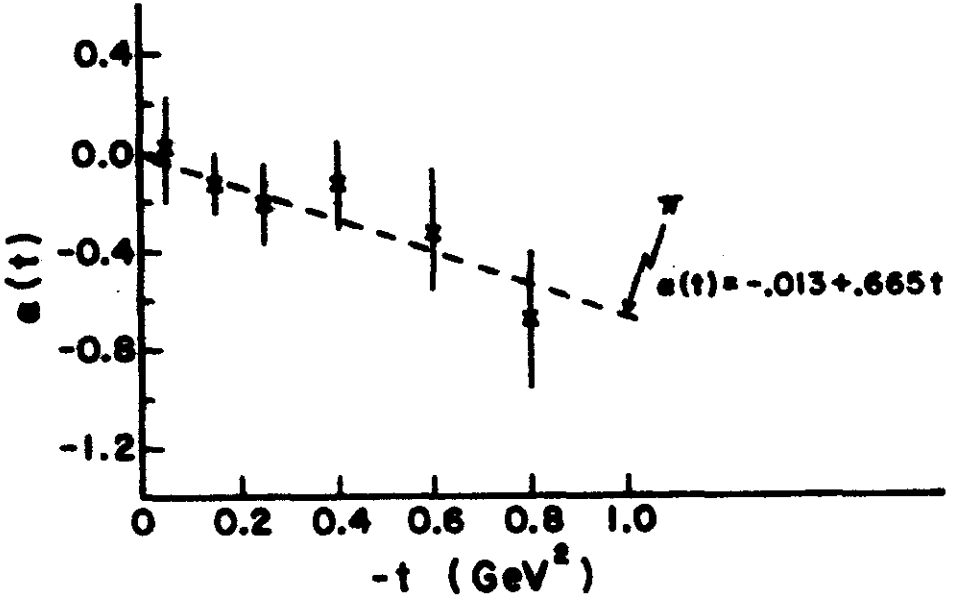
0.4
0.0
-0.4
-0.8
-1.2
0
0.2
0.4
0.6
0.8
1.0
$\alpha(t)$
$\alpha(t) = -.013 + .665t$
$-t$ (GeV^2)

Fig. 18

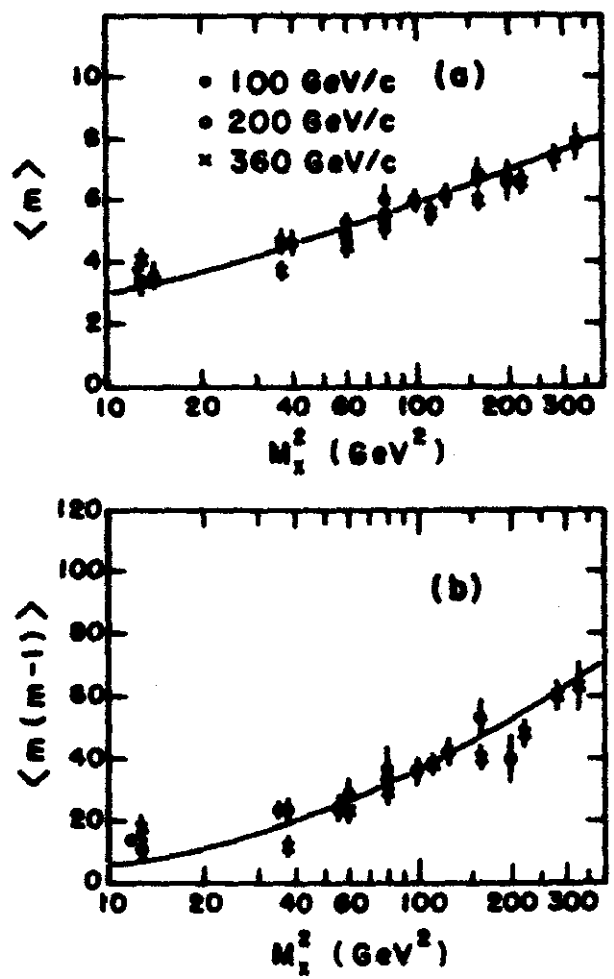

Fig. 19